VII International Conference on Computational Methods in Marine Engineering
MARINE 2017
M. Visonneau, P. Queutey and D. Le Touzé (Eds)

NUMERICAL STUDY OF CAVITATION ON A NACA0015 HYDROFOIL: SOLUTION VERIFICATION

CARLO NEGRATO*†, THOMAS LLOYD†, TOM VAN TERWISGA[II], GUILHERME VAZ[II] AND RICKARD BENSOW*

*Department of Shipping and Marine Technology
Chalmers University of Technology
Campus Lindholmen, SE-41296, Gothenburg, Sweden
email: negrato@chalmers.se - Web page: http://www.chalmers.se/

[II] Research and Development Department, †MARIN Academy
Maritime Research Institute of The Netherlands (MARIN)
P.O. 28, 6700AA, Wageningen, The Netherlands
Web page: http://www.marin.nl/

Key words: Cavitation, Verification, NACA0015 foil, RANS, Discretization Error.

Abstract. The present paper analyses a series of Computational Fluid Dynamic simulations of the cavitating flow around a two-dimensional NACA0015 foil. The foil is placed at 6° angle of attack and the cavitation number is 1.1. Two mesh designs, namely a block-structured topology and an unstructured topology, are compared; additionally, grid refinements and time step refinements are carried out. Solution Verification is addressed with calculation of the discretization error and the numerical uncertainty. The numerical uncertainty for the average lift coefficient is found to be large, up to 15%. The reason is the difficulty of achieving a grid independent solution: with very fine meshes, the flow shifts from an attached, oscillating sheet cavity pattern to a regime dominated by shedding of cavity clouds. On the other hand, neither the time resolution nor the choice of grid topology influence largely the flow pattern; instead, they only lead to differences in the maximum and minimum cavity size.

1 INTRODUCTION

The objective of Computational Fluid Dynamics (CFD) tools is to find the solution for the mathematical equations of the model which describes the flow dynamics. The governing equations are solved numerically by aid of computational resources. The numerical approach becomes necessary when the analytic solution is either unknown or impossible to determine. However, the discrete approach leads, in fact, to an approximation of the mathematical equations, hence it brings errors into the solution. Additionally, sources of errors are introduced when iterative algorithms are used to overcome the non-linearities in the model. As a result, the solution obtained from CFD codes is subject to multiple error contributions. The activity which deals

with estimation of errors and uncertainties in a numerical simulation is referred to as Solution Verification[1].

Furthermore, for practical applications, CFD codes are used to predict complex flow patterns and often involves the modeling of additional physical phenomena. This is the case for applications where hydrodynamic cavitation occurs. Cavitation is the change of phase of a flowing liquid when the local pressure falls close to the vapor pressure. Marine propellers are one example where cavitation influences the performance of the system: it affects the propeller efficiency and it can lead to undesirable effects, such as an increased noise level, induced vibrations or surface erosion. For a numerical simulation of complex flows, it becomes necessary to estimate the numerical error and provide an estimate of the uncertainty in the results; Solution Verification not only is needed to support the credibility of the numerical results, but the uncertainty level is useful when CFD is used in design tasks.

The scope of the present work is to provide Solution Verification for the cavitating flow around a NACA0015 hydrofoil. This test case has been investigated earlier, both numerically[2][3] and experimentally[4][5], but Solution Verification for the numerical calculations was not tackled so far. Furthermore, several examples of Solution Verification exercises are found in literature, for instance in the cases of cylinder flows[6]. However, to our knowledge, verification has not been addressed for a test case with unsteady cavitating flow.

The foil is placed in a water tunnel at an angle of attack of 6°. With the cavitation number equal to 1.1, the flow is unsteady. Therefore, to compute the numerical error/uncertainty, we rely on a method based on both grid and time step refinement. A series of RANS simulations is carried out with different grid densities and time steps. The large dataset allows a deeper analysis of the influence of spatial and temporal resolution. The work is complemented with a study of the effect of two different grid designs, with one set of structured grids and a second set of unstructured ones.

The paper is organized as follows: the first section explains the numerical background (§2.1), the details of the test case are given in §2.2 and a description of the method employed for calculation of errors/uncertainties is provided in §2.3. The following sections give the results of this study, with separate sub-sections regarding the numerical uncertainty (§3.1), the effect of grid design (§3.2), grid density (§3.3) and time step (§3.4). Finally, the conclusions and recommendations for future work are summarized in §4.

2 METHODOLOGY

2.1 Numerical model

The multi-phase flow is modeled using a mixture approach. The governing mass and momentum equations for an incompressible flow are solved considering the mixture density and the mixture viscosity; an additional transport equation for the vapor volume fraction α_v is added, which includes a source term to mimic the phase change. The source terms are computed by means of a modified Sauer model[7]. The turbulence modeling relies on the unsteady Reynolds-averaged-Navier-Stokes (RANS) equations, with turbulent viscosity assumption for the Reynolds stresses; all the simulations use the 2-equation k-$\sqrt{k}L$ model for turbulence closure[8].

The CFD viscous-flow code ReFRESCO (`http://www.refresco.org/`) is employed. ReFRESCO implements a finite volume, co-located discretization method, while a SIMPLE-type

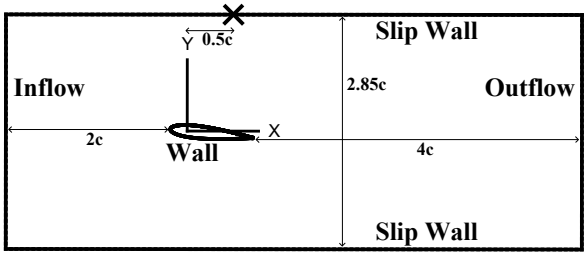

Figure 1: Domain, boundary conditions, reference system and location of the pressure probe.

algorithm is used to solve the coupled equations in a segregated manner. The convective flux in the momentum equation is discretized using a QUICK scheme. In view of the experience with simulation of cavitating flow with ReFRESCO[9] , a first-order implicit Euler scheme is used for time integration. As a result, the spatial-temporal numerical scheme is of mixed-order type[10].

2.2 Test case and computational setup

The two-dimensional NACA0015 hydrofoil has a chord length $c = 0.2\ m$ and it is placed at $\alpha = 6^\circ$ angle of attack in a water tunnel of height equals to $2.85c$ (Figure 1). A nominal width w of one chord is set. The flow domain extends $2c$ upstream of the leading edge and $4c$ downstream of the trailing edge. A pressure probe is located at the top boundary; the reference system is centered at the center of gravity of the foils (i.e. at a relative chordwise position of 0.3086). To reduce the computational cost, slip velocity is allowed at the tunnels walls. An inflow velocity $U_\infty = 6\ m/s$ results in a Reynolds number based on chord length $Re = 1.2 \cdot 10^6$, given the property of (liquid) water: $\rho_l = 998\ kg/m^3$, $\mu_l = 1.002\ kg/(ms)$. The vapor density is set to $\rho_v = 0.024\ kg/m^3$. The cavitation number is $\sigma = 2(p_{ref} - p_v)/\rho U_\infty^2 = 1.1$. The test case has been widely investigated experimentally and numerically, among others by Arndt[4] and Hoekstra[2]. The latter reports the value of $\sigma = 1.1$ as the cavitation number at which the transition occurs between a regime where an attached sheet cavity develops and a regime where shedding of cavitation clouds takes place.

Two sets of five grids each were generated. The meshing tools GridPro and Hexpress were used to create a set of block-structured grids and a set of unstructured grids respectively. The grids were designed to ensure a good resolution close to the suction side of the foil, where cavitation develops. Figure 2 gives a view of the two coarsest grids in the sets. For the unstructured grids, the cells are aligned with the undisturbed flow direction, with the exception of the boundary layer region; the coarsening towards the far field is sharper than the block-structured grid. Furthermore, the sets of structured grids are geometrical similar, which means that the grid properties (skewness, orthogonality,etc.) do not change with the grid refinement and the refinement ratio is constant over the domain. Differently, for the unstructured meshes geometrical similarity is obtained in the boundary layer cells as well as far from the foil, but in the transition region between the wall layers and the outer grid similarity is not guaranteed. All the grids were designed to fully resolve the boundary layer; the maximum value of y^+ is found at $y^+_{max} = 2.4$ and $y^+_{max} = 2.2$ for the coarse structured and coarse unstructured meshes respectively.

Table 1: Number of cells N and grid refinement ratios h_i/h_1 for the two grid sets used. Time steps t_i and time step refinement ratios t_i/t_1.

	Structured GridPro					Unstructured Hexpress				
Case ID	GP5	GP4	GP3	GP2	GP1	GH5	GH4	GH3	GH2	GH1
N ($\times 10^{-3}$)	29.6	66.3	118	263	468	26.5	83.5	171	289	437
h_i/h_1	3.97	2.66	1.99	1.33	1.00	4.06	2.29	1.60	1.23	1.00

Time steps ID	T4	T3	T2	T1
$t_i[s]$	2.667×10^{-4}	1.333×10^{-4}	6.667×10^{-5}	3.333×10^{-5}
t_i/t_1	8.00	4.00	2.00	1.00

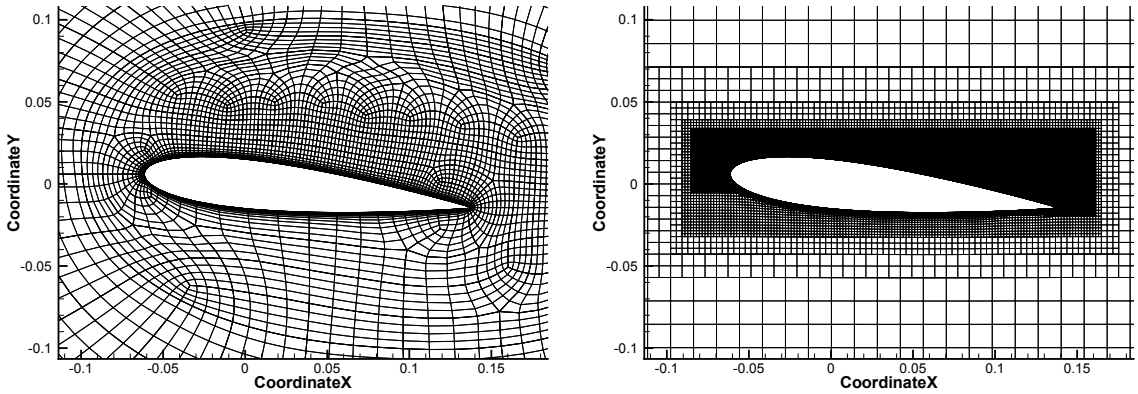

Figure 2: Overview of the coarse block-structured mesh and the coarse unstructured mesh.

Table 1 shows the number of cells and the grid refinement ratio h_i/h_1 which, for a two dimensional mesh, is defined as

$$\frac{h_i}{h_1} = \sqrt{\frac{(N_{cells})_1}{(N_{cells})_i}}, \tag{1}$$

where h_i is the typical cell size. h_1 refers to the finest mesh in the set. Efforts were put into producing grids with a comparable number of cells and similar refinement ratios between the structured the unstructured sets. Lastly, four time steps are used in combination with all the grids. The time step refinement ratio is simply the ratio of time step t_i to the finest t_1.

2.3 Solution verification

An extensive explanation of Verification & Validation tasks for CFD simulations is given by Roache[1] and summarized by Eça[11]: the scope of verification is to show that we are *"solving the equations right"*, while the scope of Validation is to show that we are *"solving the right equations"*. Following this distinction, verification provides the numerical error/uncertainties while Validation deals with the modeling error/uncertainties.

In this work, Solution Verification is provided using the method of Eça and Hoekstra[11]. One example of application of this method for unsteady flows is given by Rosetti[6]. The numerical error is commonly split into three contributions: the round-off error, the iterative error and

the discretization error. The round-off error is a consequence of the finite machine precision. The iterative error relates to the iterative methods employed to solve the non-linearity of the governing equations. While the round-off error is reduced to negligible values by use of double precision (15 digits), the iterative error can become non-negligible for complex flows. Furthermore, the cavitating flow around the hydrofoil is unsteady, hence the iterative error affects the solution at each time step. The iterative error is estimated using the infinity norm $L_\infty(\phi)$ of the normalized residuals. According to Rosetti[6], a value of $L_\infty(\phi) < 10^{-6}$ for unsteady simulations will reduce the iterative error to a negligible level. However, for the test case investigated in this study, it was not always possible to converge the simulations to this level. Some large values of $L_\infty(u_x) \approx 10^{-3}$ for the axial velocity are seen for the simulations with the finest grid and the coarsest time steps. Because in the Eça and Hoekstra method it is assumed that the discretization error is dominant, the simulations which exhibit larger residuals are discarded. In the other cases, the infinity norm is converged to values between $10^{-8} < L_\infty < 10^{-4}$, depending on the flow variable and the simulation time.

The method uses a power expansion to compute the discretization error $e(\phi_i)$ for the quantity of interest ϕ, for each case of grid&time step.[11]. There are ten error estimators featured in the Eça and Hoekstra method, which make it suitable for practical application where some scatter in the data might occur. The error estimator provides a fit through the datapoint and allows to extrapolate the exact solution. From the knowledge of the discretization error, the uncertainty is computed, which is defined as the range that contains the exact solution within a 95% accuracy. To compute the uncertainty, the method takes three factors into account: the standard deviation of the fit, the difference between the actual data point and the value obtained through the fit and a variable safety factor.

3 RESULTS

The cavitating flow over the NACA0015 was simulated with all combinations of the grids and the time steps of Table 1. As it will be shown in Section §3.3, the flow behavior depends largely on grid refinement. The flow is characterized by a sheet cavity developing at the suction side of the foil; depending on the numerical settings, the cavity either oscillates (with a periodic growth and shrinking), or it breaks up to shed a cloud which travels downstream.

In the analysis of the results, the outcome of the numerical uncertainty analysis is given in the first section. Then, the influence of spatial and temporal discretization is addressed in more detail; for the purpose, the simulation with a structured grid of approximately 118×10^3 cells and a time step of 1.333×10^{-4} (i.e. case GP3-T3) is taken as a reference.

3.1 Discretization uncertainty

The estimation of the numerical uncertainty is made for the average lift coefficient $C_L = 2L/(\rho U_\infty^2 cw)$. It is computed from the time history of the lift force in the last 12 cycles. Because of the aformentioned weaker iterative convergence for the cases with the finest grid and the coarsest time step, the solutions from the cases GP1-T4 and GH1-T4 are discarded in the error estimation.

Figure 3 shows the surface fit used to extrapolate the exact solution. Furthermore, Table 2 provides the extrapolated exact solution C_{L_0}, the error for the finest resolution $e(C_{L_1})$, the

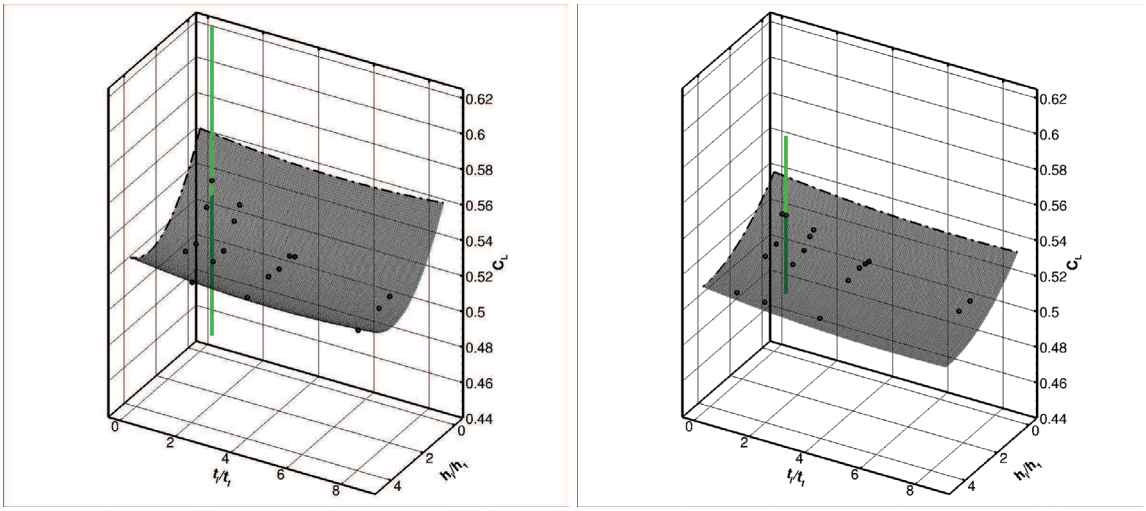

Figure 3: Values of lift coefficient from the datasets (black spheres), surface fits used for error estimation and uncertainty range (green error bars). Left: structured grid dataset. Right: unstructured grid dataset.

Table 2: Extrapolated exact solution, discretization error, uncertainty and orders of convergence. $(1, 2^*)$ indicates that a first-plus-second order fit is used, as featured in the Eça and Hoekstra method[11] .

Structured GridPro						Unstructured Hexpress					
C_{L_0}	C_{L_1}	$\frac{e(C_{L_1})}{C_{L_1}}$	U_{C_L}	p_x	p_t	C_{L_0}	C_{L_1}	$\frac{e(C_{L_1})}{C_{L_1}}$	U_{C_L}	p_x	p_t
0.564	0.549	2.7%	15%	1,2*	1,2*	0.541	0.529	2.3%	8.4%	1,2*	1,2*

numerical uncertainty and the orders of convergence. Although the percentage error for the finest simulations is <3% for both grid topologies, the uncertainty is rather large: 15% for the structured grids and 8.4% for the unstructured grid. Furthermore, the formal order of convergence (second order in space and first order in time) is not retrieved for neither dataset, which is a result of the scatter seen in the datasets.

With the fine grids, shedding of cavity clouds occurs, which does not happen with coarser grids. This additional dynamic phenomena leads to major changes on the forces exerted on the foil. Furthermore, when shedding occurs, the signal for the lift coefficient is not fully periodic, which also induces some disturbances when computing its average. The shift from a fully attached sheet to a shedding cavity regime depending on grid refinement level leads to scatter in the datasets, hence the large uncertainty values follow.

3.2 Influence of grid topology

In this section, a comparison of the reference simulation (GP3-T3) with structured grid and the simulation with unstructured grid (GH3-T3) is provided. The two cases have the same time step t_3 and the number of cells is comparable. Hence, the influence of two different topologies is

addressed. The analysis of the results is focused on the integral quantities (Table 3). Also, we look at the time traces and provide a frequency analysis (Figure 4) for three selected quantities: the total vapor volume, the lift coefficient and the pressure at the top tunnel probe. The pressure coefficient is defined as $C_p = 2p/(\rho U_\infty^2)$.

Table 3: Drag coefficient, lift coefficient and Strouhal number. Relative differences ($\Delta\star$) between the results with a structured and an unstructured grid topology are included.

Case	$\overline{C_L}$	$\Delta\overline{C_L}(\%)$	$\overline{C_D}$	$\Delta\overline{C_D}(\%)$	$\overline{C_{p_{min}}}$	$\Delta\overline{C_{p_{min}}}(\%)$	St	$\Delta St(\%)$
GP3-T3	0.520	0.48	0.0375	4.52	-1.231	1.84	0.115	-
GH3-T3	0.518		0.0358		-1.253		0.115	

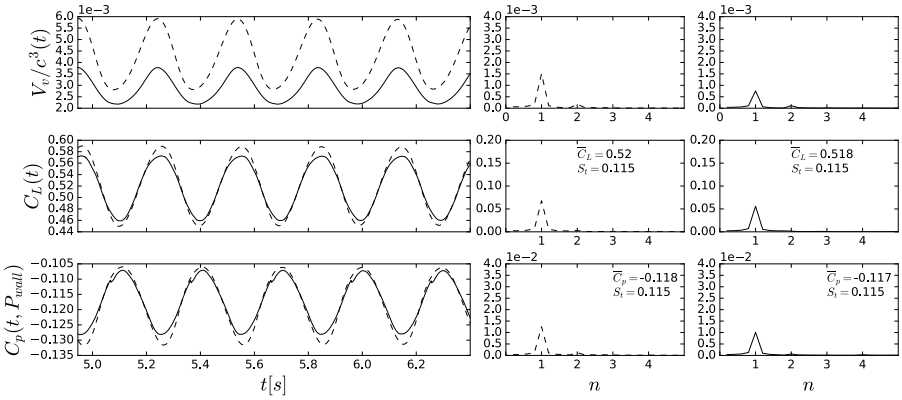

Figure 4: Time traces and harmonic contents of the total vapor volume, lift coefficient and pressure at the probe. Dashed: reference simulation GP3T3 with structured grid ($\approx 118k$ cells). Solid: unstructured grid topology, case GH3T3 ($\approx 171k$ cells). The time step is $t_3 = 1.333 \times 10^{-4}$ s for both topologies.

Finally, the Strouhal number is based on the upstream velocity and the chord length, and it is computed using the signal of the lift coefficient. The flow pattern is dominated by the growth and shrinking of an attached sheet cavity. Both topologies result in regular oscillations. The average lift coefficient differs by less than 1%, but the difference in drag coefficient is larger (4.52 %). Although the predicted frequency of cavity oscillation coincide ($St = 0.115$), the sheet cavity is longer for the structured grid during most of the cycle. Hence, the total vapor volume is larger for the structured grid, as visible in the time traces of Figure 4. However, despite the different cavity size, the instantaneous lift differs by 4% at maximum between topologies. A deeper analysis of the flow fields shows that a stronger re-entrant jet develops for the unstructured grid. The low pressure in the region of (liquid) flow where the re-entrant jet develops, partially balances the smaller cavity extension. Finally, the regular, periodic cavity oscillation is reflected in the frequency contents, where the first harmonic component is dominant for all three signals.

3.3 Influence of grid size

Secondly, the influence of grid size is investigated by a comparison between the reference solution and the solution with the finest time step in the set, i.e. $t_1 = 3.333 \times 10^{-5}$. Table 4 reports the integral values while Figure 5 gives the time histories. Furthermore, Figure 6 shows a side-by-side comparison of pressure contour plots at selected time instants. With a medium grid the attached cavity oscillates regularly between a minimum length and a maximum length, shown in the top left and bottom left plots. Remarkably, with a fine grid the predicted cavitation dynamics changes radically: a vapor structure is detached from the rear edge of the sheet cavity, as a consequence of a re-entrant jet flow which breaks up the sheet cavity. The cavity bubble is convected downstream, as shown in the two right contour plots. It moves towards the trailing edge, where it interacts with the trailing edge flow and eventually collapses downstream of the foil. Moreover, when the shed vapor structure is small, it can collapse before reaching the trailing edge. The highly dynamic cavitation cycle results in large variations of total vapor volume and lift coefficients among cycles, visible in the first time trace of Figure 5.

The largely different dynamic behavior predicted with a fine grid motivates the large differences in average loading coefficients (Table 4). The average lift coefficient differs by 4% between grids and the average drag coefficient even by 31% !

When looking at the time history, it is seen that the signals for GP1 (solid lines in Figure 5) do not show a clear period behavior. Nevertheless, the harmonic content is dominated by a first harmonic component for both the lift force and the pressure at the probe. Differently, for the total vapor volume there is no peak at the shedding frequency, but rather a broad band content in between the first harmonic $n = 1$ and the second harmonic $n = 2$.

Additionally, Figure 7 shows the average pressure coefficient distribution on the surface of the foil as well as its standard deviation. The standard deviation gives a measure of the influence of the dynamic cavitation cycle on the surface pressure. At the pressure side, the average pressure does not differ between grids. At the suction side, C_p is equal to $-\sigma$ between $-0.2 < x/c < 0.1$ for the medium grid. This is the region where the sheet cavity is continuously seen. Correspondingly, the standard deviation is zero. Furthermore, there is a quick pressure recovery in the average C_p for $x/c > 0.1$. The pressure recovery is milder for the fine grid solution because of the decrease in surface pressure induced by the cavity bubble traveling downstream. Finally, the right plot shows that the standard deviation is larger for the fine grid at both the suction side and the pressure side; the increase towards the trailing edge comes as a consequence of the interaction of the traveling bubble with the trailing edge flow. The peak is located at $x/c = 0.1$ and $x/c = 0.15$ for the medium and fine grid respectively. Because the surface pressure within the cavity is constant and equal to the vapor pressure, these chordwise coordinates represent

Table 4: Drag coefficient, lift coefficient and Strouhal number. Relative differences ($\Delta\star$) between the results with a medium grid GP3 and a fine grid GP1 are included.

Case	$\overline{C_L}$	$\Delta\overline{C_L}(\%)$	$\overline{C_D}$	$\Delta\overline{C_D}(\%)$	$\overline{C_{p_{min}}}$	$\Delta\overline{C_{p_{min}}}(\%)$	St	$\Delta St(\%)$
GP3-T3	0.520	3.58	0.0375	31.0	-1.231	2.84	0.115	9.10
GP1-T3	0.539		0.0544		-1.197		0.104	

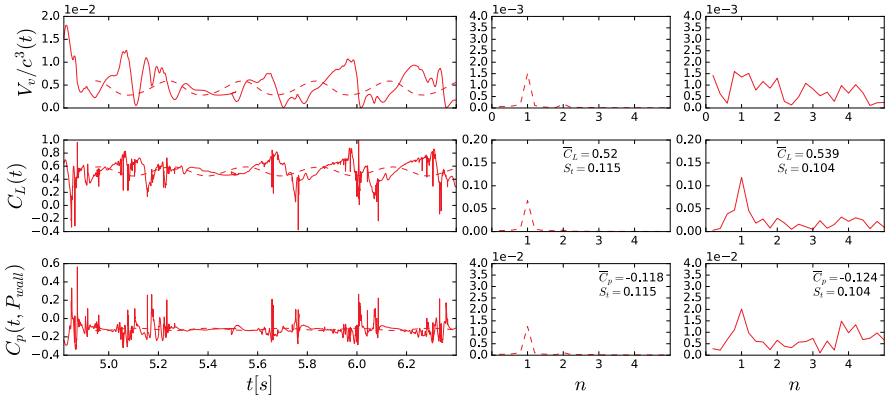

Figure 5: Time traces and harmonic contents of the total vapor volume, lift coefficient and pressure at the probe. Dashed: reference simulation with medium grid GP3 ($\approx 118k$ cells). Solid: results with fine grid GP1 ($\approx 468k$ cells). The time step is $t_3 = 1.333 \times 10^{-4}$ s for both grids.

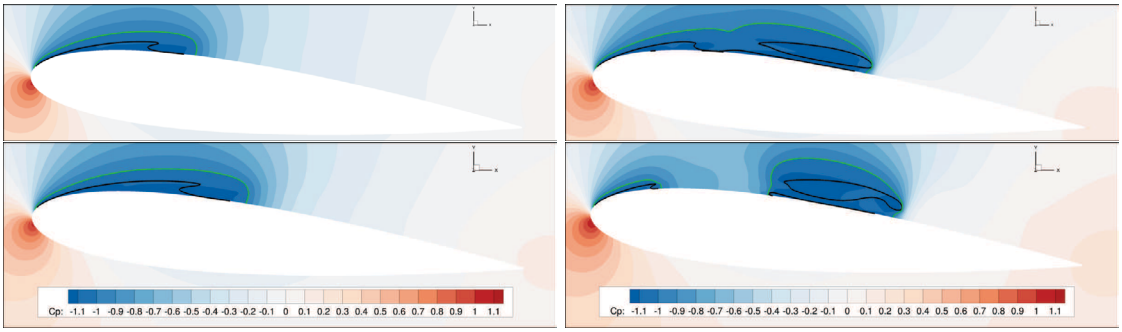

Figure 6: Contour plots of pressure coefficient. Isolines of $C_p = -\sigma = -1.1$ (green) and $\alpha_v = 0.5$ (black). Left column: reference simulation, snapshots at minimum and maximum cavity extension. Right column: snapshots with fine grid, showing the shed cavity traveling downstream during a period of time of $\approx \frac{1}{4}T_S$.

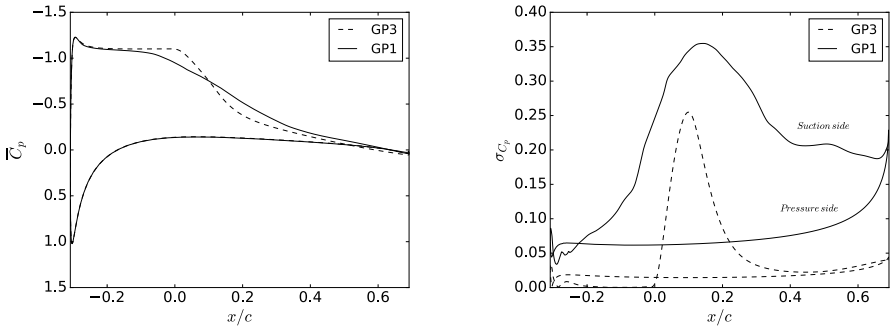

Figure 7: Average pressure coefficient distribution on the foil (left) and standard deviation (right). Dashed: reference simulation with medium grid GP3. Solid: results with fine grid GP1.

the points of maximum cavity length for the two simulations.

The change in cavitation dynamics with a fine grid is seen also with the finer time steps t_2, t_1. Besides, the same conclusions are drawn when looking at the results with the unstructured Hexpress grid topology, although the shedding behavior for the unstructured grid is less dynamic, with a more upstream and less violent collapse of the shed cavity.

3.4 Influence of time step

A third sensitivity study is carried out, regarding the effect of a change in time step while keeping the same grid resolution. The reference solution GP3-T3 with a time step $t_3 = 1.333 \times 10^{-4}$ s is compared to the solution GP3-T1 with a time step $t_1 = 3.333 \times 10^{-5}$ s. The outcome is given in Table 5 and Figure 8. Dimensionful time is used for the time traces, hence the phase shift seen is due solely to the initial, transient, part of the simulations (not shown here).

With both time steps, an attached sheet cavity remains, without shedding. The shape of the cavity is the same for the two solutions; however, with a smaller time step the attached cavity is both longer and thicker at its maximum length, which results in larger peaks in total vapor volume. In addition, a fine time step results in a smaller minimum cavity length. Correspondingly, the oscillations in lift coefficients and pressure at the top tunnel wall have larger amplitudes. Nevertheless, the difference in shedding frequency (hence the Strouhal number) is negligible.

Moreover, the frequency content of Figure 8 has a visible larger harmonic components for the solution with small time step, mostly in the second harmonic. This contribution is related to the behavior of the cavity at its early stage, when the cavity is at its minimum length: before the attached sheet cavity starts to grow again, a rapid oscillation occurs. The time scale of such effect is on the order of $10^{-2}s$, hence two to three orders of magnitude larger than the time steps. Nonetheless, only the simulation with fine time step shows this behavior.

4 CONCLUSIONS

The present work tackles the Solution Verification for the cavitating flow over a two-dimensional NACA0015 hydrofoil placed in a water tunnel at an angle of attack of 6°. The cavitation number was $\sigma = 1.1$. Multi-phase, viscous flow simulations were run using two grid topologies: a block-structured topology and a fully unstructured one. Furthermore, combinations of five systematically refined grids and four time steps were considered. Hence, it was possible to investigate the influence of discretization levels in time and space.

Discretization error and numerical uncertainty are computed. The numerical uncertainty for the average lift coefficient was found to be as large as 15% and 8.4% for the finest structured and unstructured grid respectively. The large value of the uncertainties is a consequence of scatter

Table 5: Drag coefficient, lift coefficient and Strouhal number. Relative differences ($\Delta\star$) between the results with a reference time step t_3 and a fine time step t_1.

Case	$\overline{C_L}$	$\Delta\overline{C_L}(\%)$	$\overline{C_D}$	$\Delta\overline{C_D}(\%)$	$\overline{C_{p_{min}}}$	$\Delta\overline{C_{p_{min}}}(\%)$	St	$\Delta St(\%)$
GP3-T3	0.520	3.01	0.0375	13.4	-1.231	0.05	0.115	0.01
GP3-T1	0.536		0.0433		-1.232		0.115	

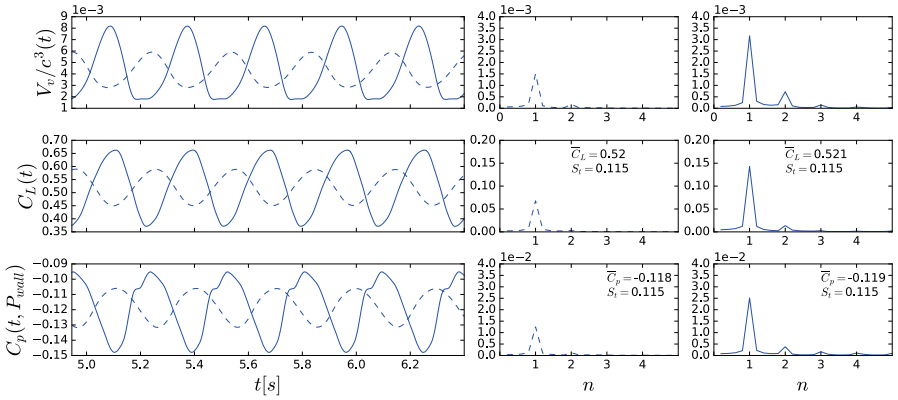

Figure 8: Time traces and harmonic contents of the total vapor volume, lift coefficient and pressure at the probe. Dashed: reference simulation with time step $t_3 = 1.333 \times 10^{-4} s$. Solid: results with fine time step $t_1 = 3.333 \times 10^{-5} s$.

in the results, due to a shift from an attached sheet cavity flow to a shedding cavity behavior for the finest spatial resolutions.

It was observed that the grid resolution has the largest influence on the flow dynamics. With a fine grid (and a medium-to-fine time step) cavity clouds are shed from the rear edge of the cavity. The clouds are convected downstream and collapses either before reaching the trailing edge or in the wake of the foil, depending on the size of the bubble. The test case is two-dimensional, and the flow modeling relies on RANS for turbulence and mixture approach for multi-phase flow. Furthermore, for the sake of the verification study, the grid densities used are rather fine, compared to what is commonly seen for unsteady RANS simulations with the same setup. Bearing in mind the assumption of the test case, the numerical settings and the level of flow modeling, it is concluded that the strive towards a grid independent solution turns out to be vain: very fine spatial and temporal resolutions leads to additional cavitation dynamics.

Finally, both the grid topology and the temporal discretization are found to provide small effects, in comparison to the large influence of grid density. With the unstructured Hexpress grids the attached sheet cavity is shorter and thinner, but the same periodic behavior of the structured GridPro grids is observed. Regarding the influence of temporal discretization, a smaller time step leads to larger oscillations of the attached sheet cavity. In addition, a small contribution from the second harmonic appears, as a result of rapid oscillation of the cavity at the beginning of the cycle, when the cavity has the minimum length. Future work is recommended to extend the current study. For the fine grids, the lack of clear periodicity is expected to affect the computation of mean values. A more thorough analysis, possibly including calculation of the statistical uncertainty, is suggested. Moreover, Solution Verification is naturally followed by Validation. In this perspective, extension to a three dimensional foil is recommended to have a more consistent comparison with the experiments.

ACKNOWLEDGEMENTS

This study was funded partly within the H2020 project LeanShips (grant no 636146) and partly within MARIN Academy funds. Simulations were performed on resources at Chalmers Centre for Computational Science and Engineering, C3SE, provided by the Swedish National Infrastructure for Computing (SNIC). The authors also wish to thank Maarten Kerkvliet (MARIN) for providing the GridPro grids.

REFERENCES

[1] Roache, P.J. Fundamentals of Verification and Validation, *Hermosa Publishers*, Albuquerque, New Mexico, (2009).

[2] Hoekstra, M. Exploratory RANS simulations of partial cavitation and its dynamics. *International conference on Computational Methods in Marine Engineering*, MARINE (2011).

[3] Yakubov, S., Maquil, T. and Rung, T. Experience using pressure-based CFD methods for Euler-Euler simulations of cavitating flows. *Computer & Fluid* 111(2015), 91–104.

[4] Arndt, R.E.A., Song, C.C.S., Kjeldsen, M., He , M. and Keller, A. Instability of partial cavitation: a numerical/experimental approach. *23rd Symp. on Naval Hydrodynamics*, Val de Reuil, France (2000).

[5] Ganesh, H., Wu, J. and Ceccio,S.L. Investigation of Cavity Shedding Dynamics on a NACA0015 Hydrofoil Using Time Resolved X-ray Densitometry. *31st Symposium on Naval Hydrodynamics*, (2016)

[6] Rosetti, G.F. , Vaz, G. and Fujarra, A.L.C. URANS Calculations for Smooth Circular Cylinder Flow in a Wide Range of Reynolds Numbers: Solution Verification and Validation. *Journal of Fluids Engineering*, Vol. 134 / 121103 (2012).

[7] Sauer, J. Instationär Kavitierende Strömungen - Ein neues Modell, basierend auf Front-Capturing(VoF) und Blasendynamik. *PhD Thesis*, University of Karlsruhe, Germany (2000).

[8] Menter, F.R., Egorov,Y. and Rush, D. Steady and unsteady flow modelling using the k-kL model. *Proc. of the International Symposium in Turbulence, Heat and Mass Transfer*. Pp. 403-406. (2006)

[9] Lloyd, T., Vaz, G., Rijpkema, D., and Schuiling, B. The Potsdam Propeller Test Case in oblique flow: prediction of propeller performance, cavitation patterns and pressure pulses. *Second International Workshop on Cavitating Propeller Performance* (2015)

[10] Roy, C.J. Grid Convergence Error Analysis for Mixed-Order Numerical Schemes. *AIAA Journal*, Vol. 41, No. 4 (2003), pp. 595-604.

[11] Eça, L. and Hoekstra, M. A procedure for the estimation of the numerical uncertainty of CFD calculations based on grid refinement studies. *Journal of computational physics*, (2014) 262, 104–130.

VII International Conference on Computational Methods in Marine Engineering
MARINE 2017
M. Visonneau, P. Queuteyand and D. Le Touzé (Eds)

EFFECTS OF BLADE GEOMETRY ON CAVITATION AND PRESSURE FLUCTUATIONS OF TUNNEL THRUSTERS

CHENG YU, XIAO-QIAN DONG*, WEI LI, CHEN-JUN YANG

State Key Laboratory of Ocean Engineering(SKLOE)
Collaborative Innovation Center for Advanced Ship and Deep-Sea Exploration(CISSE)
Shanghai Jiao Tong University, Shanghai 200240, China
*Email: xiaoqiandong0330@sjtu.edu.cn

Key words: tunnel thruster, model test, CFD, blade geometry, cavitation, fluctuating pressure

ABSTRACT: Compared with open propellers, tunnel thruster blades are more vulnerable to cavitation and local structure vibration problems because they are typically heavily loaded and subject to severe non-uniformity of inflow produced by the blunt gearbox. However, it seems that the simple 'flat plate' is still often used in designing the thruster blades. In this research, model tests and RANS simulations are carried out for three highly skewed thruster blades having different pitch and rake profiles to investigate the effects of blade geometry on cavitation and pressure fluctuations. The results indicate that the 'flat plate' blade is unfavorable for vibration excitation and unloading towards the tip is an effective way to reduce the fluctuating pressures.

1 INTRODUCTION

Ship vibration can bring about structural damage, fatigue, excessive noise and other issues. The major sources of excitation include the propeller, main engine, and waves, where the propeller is usually the most important one. Once cavitation happens, the propeller induced fluctuating pressures will increase significantly and such problems are among the most active research topics in ship propulsion.

For open propellers, relevant researches based on both model experiments and numerical simulations are relatively sufficient. For example, Pereira *et al*.[1,2] conducted fluctuating pressure and noise measurements for a cavitating propeller in uniform and non-uniform flows and demonstrated that the pressure fluctuations due to the occurrence of cavitation are proportional to the cavity volume acceleration by the test results. Salvatore *et al*.[3] compared seven computational models including RANS, LES, and BEM for the INSEAN E779A propeller in uniform and non-uniform inflows. The comparison of numerical results highlights a good agreement for the non-cavitating steady flow predictions, whereas for the cavitating flow, discrepancies in cavity extent are observed. The main reason is likely to be the lack of grid density and/or too much numerical dissipation in the vicinity of the cavity-fluid interface.

However, the relevant researches on tunnel thrusters seem to be scarcely available in the public domain due to high loading on the impeller blades and interactions among different parts of the thruster. The typical configuration of a tunnel thruster includes an impeller, a T-shaped

housing (the 'gearbox' hereinafter) of the right-angle shaft system, and a driving motor. Due to the limited space available, the gearbox is typically blunt in geometry and close to the impeller blades, which induces severe blockage effect and flow non-uniformity for the impeller. Meanwhile, the impeller blades are usually heavily loaded. Under such adverse conditions tunnel thrusters are more vulnerable to cavitation, especially when the simple 'flat plate' impeller blades are used. The fluctuating pressures induced by the impeller on the tunnel wall can exceed those by a propeller on the stern by two orders of magnitude when cavitation happens.

There are just a few pieces of work, all published in the 1960s, focusing on the hydrodynamic performance of tunnel thrusters based on model experiments[4] and design methods[5~7]. During the last ten years advances in computational fluid dynamics have made it possible to simulate the viscous flow of tunnel thrusters[8~10]. Unfortunately, the research work on cavitation and its induced effects is still scarce in the public domain. Stefano *et al*.[11] investigated the hydrodynamic performance and cavity patterns for a 'flat plate' Kaplan type propeller working in a cylinder at two pitch settings, based on BEM simulation and experimental observation. Fischer[12] proposed a design criterion for tunnel thrusters from the perspective of reducing the vibration and noise and measured the noise levels in cabins. It has been found that noise and vibration levels are different depending on thrust direction and the noise is 5~10 dB higher in low frequency range when the gearbox is located upstream of the impeller.

As dynamic positioning systems are equipped on more ships and operate more frequently, the necessity becomes obvious to enhance the performance of thrusters. In this research, model tests and RANS simulations are carried out for three highly skewed thruster blades having different pitch and rake profiles to investigate the effects of blade geometry on cavitation and pressure fluctuations. The impeller models are designed to produce the same amount of thrust when fitted to the same gearbox and bow model. The fluctuating pressures on the tunnel wall are measured at a number of locations in the vicinity of the blade tip. Viscous flow CFD simulations are carried out for the three impellers in one condition to gain more detailed information of the flow.

2 EXPERIMENTAL RESEARCH

2.1 Test facility and measuring equipments

The model tests are carried out in the cavitation tunnel of Shanghai Jiao Tong University, as shown in Figure 1. The test section is 6.1m in length, and its cross section is 1m×1m with rounded corners. The axial flow velocity over the test section ranges from 0.5m/s to 15.8m/s, and the static pressure at the centerline of the test section ranges from 25kPa to 300kPa. The non-uniformity of axial flow velocity is less than 1%.

As shown in Figure 2, the generic bow model is 0.58m long, with identical cross section geometry over the length and a tunnel in transverse direction to house the thruster. The bow model is made of plexiglass to facilitate observation of the flow and cavitation inside the tunnel. As illustrated in Figure 3, the bow model is installed at the streamwise center of the third